Check for updates

ChemElectroChem

Research Article
doi.org/10.1002/celc.202400699

Chemistry Europe
European Chemical Societies Publishing

www.chemelectrochem.org

Electrooxidation of 2-Propanol on Mono- and Bi-Metallic Noble Metal Nanoparticles in Alkaline Studied with Real-Time Product and Dissolution Characterization

Iosif Mangoufis-Giasin,*[a, b] Attila Kormányos,[a, c] Mária Minichová,[a, b] Andreas Körner,[a, b] Birk Fritsch,[a] Karl J. J. Mayrhofer,[a, b] Serhiy Cherevko,[a] and Ioannis Katsounaros*[a, d]

The selective electrochemical oxidation of 2-propanol to acetone can be used in fuel cells to deliver low-carbon electricity and efficiently utilize hydrogen that is stored in liquid organic hydrogen carrier molecules. Here we study the electrooxidation of 2-propanol in alkaline electrolyte, on various commercially available carbon-supported mono- and bi-metallic noble metal nanoparticles. We use voltammetry to compare the activity of different catalysts, and we combine a flow cell with real-time analytics to monitor the products of the reaction and the dissolution of metal atoms in the presence and absence of 2-propanol. While acetone if formed on all catalysts, our results show that the onset potential is the lowest for PtRu/C, Rh/C and PdRh/C, but the oxidation current for the latter reaches a much higher value before the surface is passivated, suggesting that PdRh/C would be preferred in an alkaline fuel cell that is fed with 2-propanol. Online dissolution monitoring suggests that the anode in a 2-propanol fuel cell should not be exposed to potentials above ca. +0.8 V during transient operation, i.e., during startup/shutdown conditions, to prevent dissolution of palladium and rhodium from the catalyst surface.

Introduction

Liquid organic hydrogen carriers (LOHCs) can be a solution to the major challenges associated with hydrogen storage and transportation on a large scale, and thus they can significantly contribute to a hydrogen-based economy. LOHCs can store hydrogen into hydrogen-carrying organic molecules at the point of H_2 production and be distributed safely at the point of use, where hydrogen can be thermally released.[1] Such hydrogen loading/unloading cycles between LOHC molecules, for example between dibenzyltoluene (H0-DBT) and perhydrodibenzyltoluene (H18-DBT), can be repeated without noticeable stability issues.[2] Therefore, they can act as excellent hydrogen storage media while offering significant advantages over pressurized hydrogen due to their comparably low cost, high volumetric energy storage density, safe handling at ambient conditions and high compatibility with the existing infrastructure from fossil fuels.[1,3]

When the goal is to produce electricity using H_2 that is stored in LOHCs, the combination of the endothermic LOHC dehydrogenation with a power generating device leads to significant losses in the (LOHC-bound) hydrogen-to-electricity efficiency.[4] Heat integration between a hydrogen fuel cell and the LOHC dehydrogenation reactor would be a way to improve efficiency, but polymer electrolyte membrane fuel cells (PEMFCs) operate at considerably lower temperatures than those required for H_2 release from LOHCs (in the order of 300 °C),[2] whereas the combination with high-temperature, e.g. solid-oxide fuel cells (SOFCs)[5] will be difficult to deploy at scale – even more for applications under dynamic operation.

A concept for the production of electricity using LOHC-bound hydrogen was described in a previous publication.[4] This is based on the hydrogenation of acetone from the hydrogen-rich alicyclic liquid (Hx-LOHC) via thermoneutral catalytic transfer hydrogenation reaction (CTHR). The formed gaseous 2-propanol/acetone mixture is separated and acetone is recycled back to the transfer hydrogenation unit, whereas 2-propanol is fed to a PEMFC to produce electricity.[4] The main advantage that the pair acetone/2-propanol offers over the traditional alcohol fuel cells (e.g. based on methanol or ethanol) for integration with the LOHC technology is the difficulty in breaking the C–C bond of the secondary alcohol and the subsequent absence of CO_2 formation, during the alcohol oxidation reaction.[6] Thus, the produced acetone can be recycled back to the CTHR and undergo another CTHR-PEMFC cycle. In acidic conditions, only platinum and platinum-based

[a] I. Mangoufis-Giasin, A. Kormányos, M. Minichová, A. Körner, B. Fritsch, K. J. J. Mayrhofer, S. Cherevko, I. Katsounaros
Helmholtz Institute Erlangen-Nürnberg for Renewable Energy (IET-2), Forschungszentrum Jülich GmbH, Cauerstr. 1, 91058 Erlangen, Germany
E-mail: iosif.mangoufis@fau.de
katsounaros@chem.auth.gr

[b] I. Mangoufis-Giasin, M. Minichová, A. Körner, K. J. J. Mayrhofer
Department of Chemical and Biological Engineering, Friedrich-Alexander-Universität Erlangen-Nürnberg, Immerwahrstraße 2a, 91058 Erlangen, Germany

[c] A. Kormányos
Department of Physical Chemistry and Materials Science, University of Szeged, Rerrich Square 1, Szeged H-6720, Hungary

[d] I. Katsounaros
Department of Chemistry, Aristotle University of Thessaloniki, 54124 Thessaloniki, Greece

Supporting information for this article is available on the WWW under https://doi.org/10.1002/celc.202400699

© 2025 The Authors. ChemElectroChem published by Wiley-VCH GmbH. This is an open access article under the terms of the Creative Commons Attribution License, which permits use, distribution and reproduction in any medium, provided the original work is properly cited.

© 2025 The Authors. ChemElectroChem published by Wiley-VCH GmbH

alloy electrocatalysts show activity towards 2-propanol electrooxidation, with acetone being the sole product.[7–13] The absence of CO_2 formation is further supported by spectroscopic studies alongside the lack of CO formation, as an absorbed intermediate.[14–17] In fact, the selective formation of the respective ketone is a general characteristic of the secondary alcohols electrooxidation.[18,19]

On the contrary, a broader range of electrodes shows activity for the 2-propanol electrooxidation in alkaline media, apart from platinum-based electrocatalysts, such as rhodium, palladium, gold and nickel.[13,20,21–29] Moreover, enhanced electrocatalytic activities were observed previously for some platinum- and palladium-based electrocatalysts.[30–39]

In a recent publication, we showed that the activity for four polycrystalline noble metal electrodes (Rh, Pt, Pd, and Au) in alkaline solutions is correlated to the adsorption energy of acetone, which was the sole product of the electrooxidation process.[13] Polycrystalline rhodium exhibited a low onset potential, whereas a high current density was observed for a palladium disk. Based on this observation, here we examine the activity, selectivity and stability of palladium, rhodium, and palladium-rhodium (1:1) nanoparticles supported on carbon (Pd/C, Rh/C, and PdRh/C). Platinum-ruthenium (PtRu/C, 1:1), the state-of-the-art electrocatalyst in acidic conditions, is used as a reference catalyst in alkaline, alongside the respective carbon-supported monometallic nanoparticles, platinum and ruthenium (Pt/C and Ru/C). We compare the activity of different catalysts for 2-propanol electrooxidation in alkaline, together with a geometric estimation of each respective surface area. Besides the classical electrochemical characterization, here we follow the tolerance of all materials to acetone poisoning by combining chronoamperometric steps with real-time product monitoring, whereas we also perform electrochemical online dissolution studies on the bimetallic catalysts, and we find that exposure to high potentials during startup/shutdown or uncontrolled idle (e.g. 2-propanol starvation, oxygen diffusion to anode etc.) conditions of a 2-propanol alkaline fuel cell is detrimental to catalyst stability. We eventually propose that PdRh/C is the most promising catalyst (in terms of performance) as an anode in a 2-propanol alkaline fuel cell. However, if such an LOHC technology coupled to 2-propanol fuel cells is deployed in the future, the contribution of the high cost of PdRh/C to the total capital expenditure will need to be thoroughly evaluated.

Materials and Methods

Electrocatalyst Thin-Film Preparation

All electrocatalysts used in this study (Pt/C, Ru/C, PtRu/C, Pd/C, Rh/C, and PdRh/C) were commercial nanoparticles from Fuel Cell Store (FCS) and Tanaka Kikinzoku Kogyo (TKK); details on the catalyst characteristics, as provided by the manufacturer, are summarized in Table 1. The nanoparticles were dispersed using an SFX150 Horn Sonifier (Branson, USA), in ultrapure water with addition of 2-propanol (water:2-propanol volume ratio 3:1). From the resulting homogeneous catalyst ink, 20 μL were pipetted onto a glassy carbon disk (embedded on Teflon shroud, PINE) for rotating disk electrode (RDE) measurements, 3 μL on a glassy carbon plate (HTW Hochtemperatur-Werkstoffe GmbH) for electrochemical real-time mass spectrometry (EC-RTMS), and 0.2 μL on a glassy carbon plate (SIGRADUR 5 cm×5 cm) for electrochemical online dissolution measurements. The drop-casted suspension was left to dry in air, resulting in a thin catalyst film on the substrate, which acted as the working electrode; the final total metal loading was 25 $\mu g\,cm^{-2}$ for RDE and EC-RTMS measurements, and 20 $\mu g\,cm^{-2}$ for the electrochemical dissolution studies. The homogeneity of the coating and the exact diameter of each catalyst spot was scrutinized by a laser scanning microscope (Keyence VK-X250) and ranged between 350–450 μm in radius. All glassy carbon substrates (disks or plates) were polished before each deposition with diamond pastes (grain sizes of 3, 1 and 0.25 μm, Saint-Gobain Diamantwerkzeug GmbH) and subsequently were sonicated in ultrapure water, 2-propanol and ultrapure water successively (15 min in each step).

RDE Measurements

Unless complementary product analysis was performed, linear sweep voltammetry was recorded in an RDE setup, using a custom-made three-compartment/electrode Teflon cell and a PINE MSR Electrode Rotator. The counter electrode was a platinum wire (Mateck GmbH), and the reference electrode was a Ag/AgCl in 3.0 $mol\,L^{-1}$ KCl (Metrohm). All potentials in the manuscript are expressed with respect to the reversible hydrogen electrode (RHE), determined by measuring the open circuit potential of a platinum wire versus the Ag/AgCl reference electrode in a hydrogen-saturated 0.1 $mol\,L^{-1}$ NaOH solution. A Gamry Reference [600] potentiostat/galvanostat was used for all measurements. The electrolyte resistance was determined before each measurement with electrochemical impedance spectroscopy and compensation (by 90%) was performed using the positive feedback mode; the remaining uncompensated resistance was always below 4 Ω. The electrolyte was prepared by dissolving NaOH pellets (EMSURE for analysis, Supelco) and 2-propanol (Merck Suprapure) in ultrapure water (Merck Millipore, resistance 18.2 MΩ cm, total organic carbon – TOC < 5 ppb at 25 °C). All glassware and Teflon parts used in the electrochemical experiments were cleaned by storing them in sulfuric acid (98%, Merck) with NOCHROMIX® (Sigma Aldrich) for at

Table 1. Specifications of the tested electrocatalysts, as provided by each respective manufacturer. The TEM particle size values were obtained internally.

Electrocatalyst/Product Name	Carbon Support	Nominal Atomic Ratio	Total Metal Loading/wt.%	TEM–Particle Size/nm
Pt/C-TKK/TEC10E40E	High Surface Area Carbon	–	36.8	1.90 ± 0.57
Ru/C-FCS/57080103	Vulcan XC-72	–	20	2.08 ± 0.62
PtRu/C-TKK/TEC66E50	High Surface Area Carbon	1:1	49.7	2.38 ± 1.00
Pd/C-FCS/57080053	Vulcan XC-72	–	20	2.74 ± 0.77
Rh/C-FCS/57080101	Vulcan XC-72	–	20	2.37 ± 0.65
PdRh/C-FCS/- (custom order)	Vulcan XC-72	1:1	20	2.46 ± 0.58

© 2025 The Authors. ChemElectroChem published by Wiley-VCH GmbH

21960216, 2025, 9, Downloaded from https://chemistry-europe.onlinelibrary.wiley.com/doi/10.1002/celc.202400699 by Forschungszentrum Jülich GmbH Research Center, Wiley Online Library on [08/12/2025]. See the Terms and Conditions (https://onlinelibrary.wiley.com/terms-and-conditions) on Wiley Online Library for rules of use; OA articles are governed by the applicable Creative Commons License

21960216, 2025, 9, Downloaded from https://chemistry-europe.onlinelibrary.wiley.com/doi/10.1002/celc.202400699 by Forschungszentrum Jülich GmbH Research Center, Wiley Online Library on [08/12/2025]. See the Terms and Conditions (https://onlinelibrary.wiley.com/terms-and-conditions) on Wiley Online Library for rules of use; OA articles are governed by the applicable Creative Commons License

least 12 h, rinsing and subsequently boiling three times with ultrapure water.

EC-RTMS Measurements

Product analysis by EC-RTMS was performed using a V-type flow cell (scanning flow cell, SFC) coupled to direct analysis in real time - time of flight - mass spectrometer (DART-TOF-MS). The basic principles of EC-RTMS for the real-time characterization of electrolyte composition have been described in detail by Khanipour et al.[40] In brief, a collection capillary was positioned close (ca. 100 μm) to the surface of the working electrode, and the electrolyte along with the reaction products were continuously withdrawn for analysis with DART-TOF-MS (JEOL JMS-T100LP AccuTOF). The dissolved acetone formed after the oxidation of 2-propanol was analyzed in the negative mode, at the mass range m/z = 58.0–58.1 (ion structure $[^{13}C^{12}C_2H_6O\text{-}H]^-$). The counter electrode (Pt wire, Mateck GmbH) was placed at the waste channel of the SFC, i.e. separately from the collection capillary, to avoid any interference with the product analysis. The reference electrode was a Ag/AgCl in 3.0 mol L^{-1} KCl (BASi). A Gamry Reference [600] potentiostat/galvanostat was used for all measurements. The electrolyte, introduced continuously in the flow cell from an FEP canister, was purged with Argon (Air Liquide, 4.8 N) prior to each measurement for 20 min, and the gas flow was then maintained throughout the entire experiment.

Dissolution Studies Using Online Inductively Coupled Plasma Mass Spectrometry (ICP-MS)

The stability of the carbon-supported bimetallic alloys was quantified in-situ by the SFC, in which the outlet was coupled to an on-line ICP-MS (PerkinElmer, Nexion 300X). A Ag/AgCl 3 mol L^{-1} KCl electrode (Metrohm) was used as the reference electrode, which was introduced in the outlet of the SFC via a capillary channel. A glassy carbon rod (SIGRADUR) was employed as the counter electrode, which was connected to the cell on the electrolyte inlet side. The glassy carbon plate along with the drop-casted spots served as the working electrode. The working electrode was placed on a 3D translational stage (Physik Instrumente M-403), which allowed easy and rapid navigation between the different samples. A detailed description of the complete setup is available elsewhere.[41,42] All dissolution data in the manuscript have been normalized by the individual geometric surface area.

All electrochemical measurements were carried out using a Gamry Reference [600] potentiostat/galvanostat. Electrocatalyst stability was scrutinized by performing the following protocol either in 0.05 mol L^{-1} KOH or in 0.05 mol L^{-1} KOH + 0.05 mol L^{-1} 2-propanol electrolyte solutions, saturated with Ar during the measurement: first, the potential was held at 0 V_{RHE} for 5 min; then, three consecutive cyclic voltammograms with gradually increasing upper potential limits (+1, +1.1, and +1.2 V_{RHE}) were recorded with a scan rate of 10 mV s^{-1}. Salt and organic content of the electrolyte had to be kept around 2 wt% due to the limitation of the ICP-MS: higher concentrations could precipitate and clog the nebulizer of the device or precipitate and (partially) block the sampling cones of the device. The protocol was concluded with a 3 min potentiostatic hold at 0 V_{RHE} to allow the ICP-MS signal to return to its baseline value.

ICP-MS calibration was performed daily prior to the measurements, with a four-point calibration curve made from standard solutions (Merck Certipur, Pd, Rh, Pt, and Ru) containing the metal ions of interest in a given concentration in 0.05 mol L^{-1} KOH (+0.05 mol L^{-1} 2-propanol) electrolyte solution. ^{130}Te (for ^{108}Pd), ^{115}In (for ^{103}Rh), ^{187}Re (for ^{195}Pt), and ^{103}Rh (for ^{102}Ru) were used as internal standards. Internal standard solutions were prepared in 1 wt% HNO_3 electrolyte and were introduced in the sample stream via a Y-connector. The purged electrolyte flow rate was controlled by the peristaltic pump of the spectrometer (M2, Elemental Scientific). The average flow rate was 3.50 ± 0.05 μL s^{-1}.

Transmission Electron Microscopy (TEM)

The sample particle size and distribution on carbon support was investigated with TEM. Sample powders were suspended in water:2-propanol (volume ratio 1:1) mixture and sonicated for 5 min before TEM grids were dip-coated. Consecutively, the grids dried under air atmosphere and cleaned for 1 min with air plasma by using a Tergeo EM plasma cleaner (PIE Scientific). TEM micrographs were acquired using a Talos F200i (Thermo Fisher Scientific). The microscope was operated at an acceleration voltage of 200 kV and is equipped with a Schottky emitter. The particle size distribution was determined from the 2D TEM images by using the open-source software Fiji. The reported particle size corresponds to the equivalent projected area diameter, calculated as the diameter of a circle that has the same area as the particle 2D-projected area (equivalent sphere concept).[43]

Results and Discussion

Voltammetric Characterizations and TEM Surface Area Determination

The positive-going linear sweep voltammograms in 0.1 mol L^{-1} NaOH electrolyte with 0.2 mol L^{-1} 2-propanol on mono- and bimetallic nanoparticles supported on carbon (Pd/C, Rh/C, PdRh/C, Pt/C, Ru/C, and PtRu/C) are shown in Figure 1. The oxidation peaks along the potential window on different electroactive surfaces are attributed solely to 2-propanol electrooxidation, as can be easily extracted by the comparison with the "blank voltammograms" in the absence of 2-propanol, available in Figure S1–1, in the supporting information (SI). The lowest onset potential (ca. +0.1 V_{RHE}) is observed for Rh/C, PdRh/C and

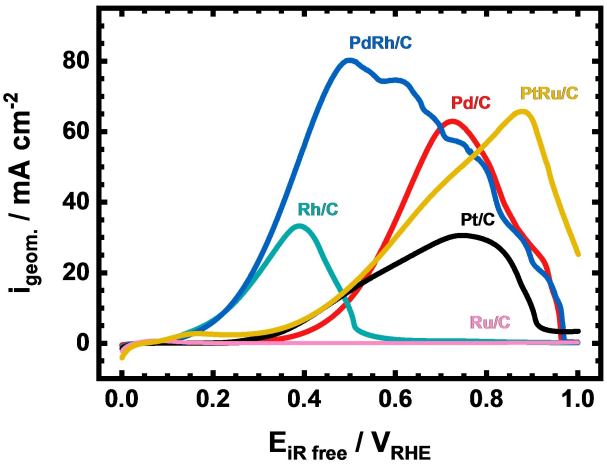

Figure 1. Electrooxidation of 2-propanol on Pd/C, Rh/C, PdRh/C, Pt/C, Ru/C and PtRu/C nanoparticles. Positive-going LSVs in 0.1 mol L^{-1} NaOH and 0.2 mol L^{-1} 2-propanol. Total metal loading: 25 μg cm^{-2}. Scan rate: 5 mV s^{-1}. Rotation speed: 1600 rpm.

© 2025 The Authors. ChemElectroChem published by Wiley-VCH GmbH

PtRu/C, which is close to the thermodynamic equilibrium potential for the acetone/2-propanol redox couple (+0.13 V at standard conditions).[4] Pt/C (ca. +0.25 V_{RHE}) and Pd/C (ca. +0.3 V_{RHE}) activate 2-propanol at higher overpotentials, whereas Ru/C shows no activity, similarly to acidic conditions.[7] Thus, Ru/C is not further used in the analysis presented below. The maximum current density was recorded for PdRh/C (ca. 80 mA cm^{-2}), followed by the other electrocatalysts along the series PtRu/C (ca. 66 mA cm^{-2}) < Pd/C (ca. 63 mA cm^{-2}) < Rh/C (ca. 34 mA cm^{-2}) < Pt/C (ca. 31 mA cm^{-2}).

The electrooxidation of 2-propanol on PtRu/C in alkaline conditions takes place in two potential regions (1st peak onset at ca. +0.1 V_{RHE}/2nd peak onset at ca. +0.25 V_{RHE} with peak potential at ca. +0.85 V_{RHE}), similarly to what was shown for acidic media by Khanipour et al.[7] We have previously attributed the first peak to 2-propanol oxidation on Pt–Ru ensemble sites, and the second peak to oxidation solely on Pt.[18] A different explanation is provided by Simanenko et al., as the origin of the first oxidation peak is attributed to the formation of ultra-small Pt aggregates on top of rough Ru surface and not on Pt–Ru ensemble sites.[44] Note that the early onset at ca. +0.1 V_{RHE} is not observed for the monometallic catalysts, Pt/C and Ru/C. For the second oxidative process, a discrepancy is observed between acidic and alkaline conditions with regard to the peak potential and peak current density. Whereas, in acidic conditions the peak potential and the respective current density peak are almost similar for Pt/C and PtRu/C (same Pt loading in Khanipour's study, 25 μg cm^{-2}), in alkaline electrolyte, the peak is shifted to higher potentials for PtRu/C (ca. +0.85 V_{RHE} versus ca. +0.75 V_{RHE} for Pt/C). This is accompanied by a more than double increase in peak current density for PtRu/C compared to Pt/C, although the Pt loading is lower (16.47 μg_{Pt} cm^{-2} for PtRu/C < 25 μg_{Pt} cm^{-2} for Pt/C). Those characteristics may either indicate that the reaction follows a different mechanism or derive from the differences in oxide formation between PtRu/C and Pt/C surfaces respectively. Nevertheless, on both surfaces a change in voltammetry curve is observed between +0.5 and +0.75 V_{RHE}, which is attributed by Markiewicz et al. to two different 2-propanol oxidation mechanisms due to changes in surface oxidation state and subsequently in strongly absorbed intermediates that poison the surface at each potential window.[20]

Analogously, PdRh/C also exhibits enhanced performance in comparison to the respective single-metal nanoparticles. The onset potential for PdRh/C coincides with that of Rh/C. However, while the current for the latter is maximized at ca. +0.4 V_{RHE} (ca. 34 mA cm^{-2}), a broad oxidation peak is observed for PdRh/C, ranging from the onset potential of Rh/C to the deactivation potential of Pd/C. Eventually, the 2-propanol oxidation on the PdRh/C electrode rate reaches ca. 80 mA cm^{-2} at the peak potential of ca. +0.5 V_{RHE}.

Differences in the recorded current densities could have originated from differences in particle size and the resulting surface area. Given that it is not straightforward to measure the electrochemically active surface area of all materials under study with conventional stripping methods (e.g., underpotential deposited hydrogen or CO stripping), we made an estimation based on the particle size of the respective material. To this end, TEM images were obtained for all materials and are shown in Figure 2 alongside the respective particle size distribution histograms (enlarged TEM images in Figure S2 of the SI). To obtain the necessary quantitative information for each catalyst, the number ($\overline{d_N}$) and the volume-surface area ($\overline{d_{V/a}}$) average diameters were determined from the Equations (1–2) by using the measured diameters (d_i) of 300 nanoparticles (n) per catalyst from several TEM images, as described by Loichet Torres et al.:[45]

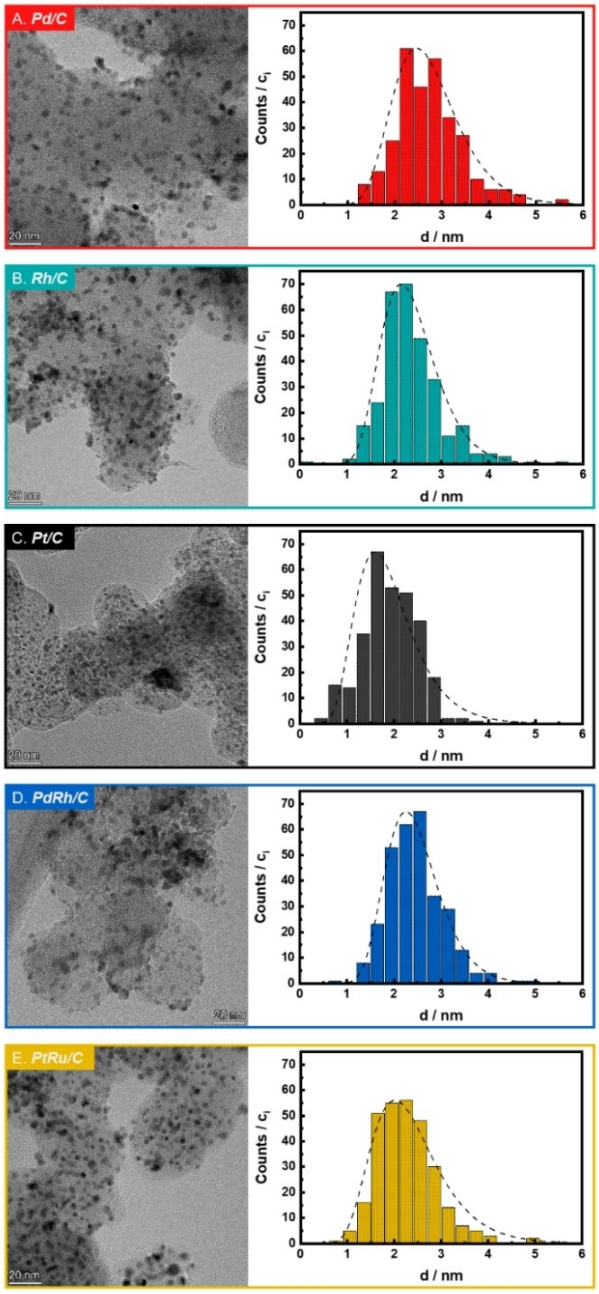

Figure 2. Typical TEM images of supported nanoparticles of (A) Pd/C, (B) Rh/C, (C) Pt/C, (D) PdRh/C and (E) PtRu/C and the respective particle size distribution histograms. Enlarged TEM images in Figure S2 of the SI.

© 2025 The Authors. ChemElectroChem published by Wiley-VCH GmbH

21960216, 2025, 9, Downloaded from https://chemistry-europe.onlinelibrary.wiley.com/doi/10.1002/celc.202400699 by Forschungszentrum Jülich GmbH Research Center, Wiley Online Library on [08/12/2025]. See the Terms and Conditions (https://onlinelibrary.wiley.com/terms-and-conditions) on Wiley Online Library for rules of use; OA articles are governed by the applicable Creative Commons License

$$\overline{d_N} = \frac{\sum_{i=1}^{n} d_i}{n} \quad (1)$$

$$\overline{d_{V/a}} = \frac{\sum_{i=1}^{n} d_i^3}{\sum_{i=i}^{n} d_i^2} \quad (2)$$

All materials show similar $\overline{d_N}$ and $\overline{d_{V/a}}$ values that range roughly in a narrow window between 2and 3.5 nm. Additionally, in Figure 3 the TEM-derived surface area (SA_{TEM}) of the nanoparticles is extracted based on the calculated $\overline{d_{V/a}}$ by Equation (3) and the corresponding crystallographic densities (ρ_x) (i.e. $\rho_{Pt} = 21.4\ g\,cm^{-3}$, $\rho_{Ru} = 12.3\ g\,cm^{-3}$, $\rho_{Pd} = 12.02\ g\,cm^{-3}$ and $\rho_{Rh} = 12.44\ g\,cm^{-3}$).[46–48] The alloy density ($\rho_{M_1M_2}$) is calculated by Equation (4):

$$SA_{TEM} = \frac{6}{\overline{d_{V/a}} \cdot \rho_x} \quad (3)$$

$$\rho_{M_1M_2} = y_{M_1}\rho_{M_1} + y_{M_2}\rho_{M_2} \quad (4)$$

where y is the mass fraction of each metal.

The SA_{TEM} values for Pd/C, Rh/C, PdRh/C (ca. 155–179 $m^2_{metal}\,g^{-1}_{metal}$) show that the expected differences in surface area are not significant enough to explain the difference in recorded current densities. Particularly, the SA_{TEM} difference between Rh/C and PdRh/C (<2%) alongside the fact that the PdRh/C oxidation peak, at the potential window from +0.1 to +0.5 V_{RHE}, is broad and unaffected by the RhO_x formation[49] indicates an enhanced catalytic performance due to the alloying between Pd and Rh. Similarly, Pt/C shows a SA_{TEM} value (ca. 127 $m^2_{metal}\,g^{-1}_{metal}$) greater than PtRu/C (ca. 92 $m^2_{metal}\,g^{-1}_{metal}$), although the current density for the latter catalyst at the potential window from +0.5 to +1 V_{RHE} is higher. We conclude that both PdRh/C and PtRu/C, in this study, are more active in alkaline electrolyte compared to the individual monometallic catalysts, which is attributed to intrinsic characteristics of each alloy and not to differences in particle size or surface area.

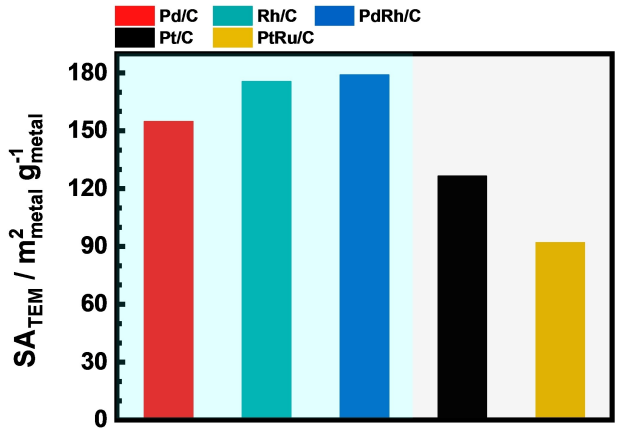

Figure 3. TEM-derived surface area values in $m^2\,g^{-1}$ for Pd/C, Rh/C, PdRh/C, Pt/C and PtRu/C nanoparticles.

To understand further the potential dependence of 2-propanol electrooxidation on the different electrocatalysts in alkaline media, the LSVs with and without the presence of 2-propanol were compared (Figure 4, i.e., a closer inspection of the blank voltammograms in Figure S1–2 in the SI). Overall, the oxidation current of 2-propanol reaches a maximum and then decreases, until the reaction practically ceases at a potential range where either the adsorption of oxygenated species from the electrolyte (e.g. OH_{ads}) or the oxide formation takes place on each respective surface. Previous studies have shown that surface changes that are attributed to oxygenated species or oxides formation in alkaline electrolytes take place for polycrystalline Pd, Rh and Pt at a potential window similar to our study (Pd ca. +0.2 V_{RHE}, Rh ca. +0.35 V_{RHE} and Pt ca. +0.45 V_{RHE}).[49–51]

In particular, the current density for 2-propanol oxidation on Rh/C is maximized at ca. +0.35 to +0.4 V_{RHE}, where a feature emerges in the blank voltammogram which is related to the commencement of Rh oxide formation in alkaline media.[49] The oxidation rate on Pd/C is maximized at a potential close to ca. +0.7 V_{RHE}, where the formation of the Pd (II) oxide layer takes place, as can be also seen by the respective features that emerge in the blank solution.[52] Accordingly, the electrocatalytic activity of Pt/C for 2-propanol oxidation decreases at ca. +0.7 to +0.75 V_{RHE}, where the convoluted formation of both Pt^{δ}-OH_{ads} ($0 < \delta < 1$) and Pt (II) oxide initiates.[53,54]

The current profiles for the two bimetallic materials, PdRh/C and PtRu/C, compared to the respective monometallic catalysts, can be associated with the differences in blank voltammograms

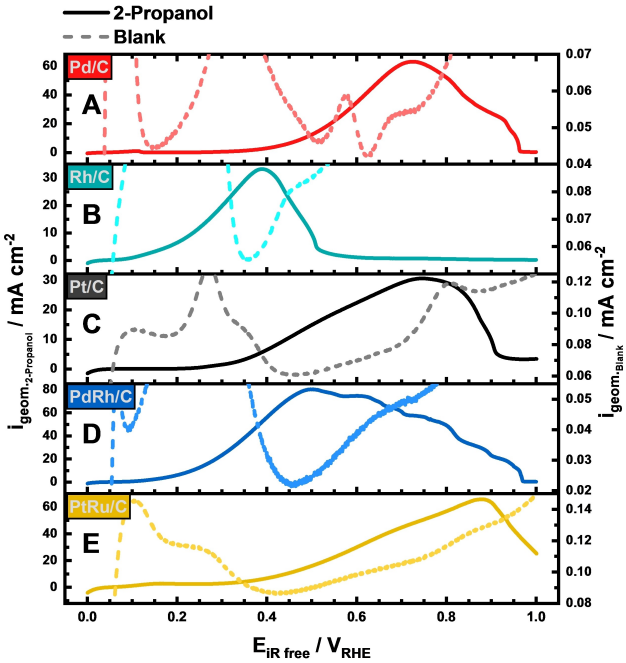

Figure 4. Positive-going LSVs in 0.1 mol L^{-1} NaOH (blank) and 0.1 mol L^{-1} NaOH/0.2 mol L^{-1} 2-propanol solutions of (A) Pd/C, (B) Rh/C, (C) Pt/C, (D) PdRh/C and (E) PtRu/C nanoparticles. Total metal loading: 25 $\mu g\,cm^{-2}$. Scan rate: 5 $mV\,s^{-1}$. Rotation speed: 1600 rpm. Note the different scales of current density for the solution with 2-propanol (left Y-axis) and without 2-propanol (right Y-axis).

© 2025 The Authors. ChemElectroChem published by Wiley-VCH GmbH

21960216, 2025, 9, Downloaded from https://chemistry-europe.onlinelibrary.wiley.com/doi/10.1002/celc.202400699 by Forschungszentrum Jülich GmbH Research Center, Wiley Online Library on [08/12/2025]. See the Terms and Conditions (https://onlinelibrary.wiley.com/terms-and-conditions) on Wiley Online Library for rules of use; OA articles are governed by the applicable Creative Commons License

between the materials. For example, the oxide formation on PdRh/C (ca. +0.45 V_{RHE}) is shifted by ca. 100 mV compared to Rh/C (ca. +0.35 V_{RHE}) in blank voltammetry, and the peak potential for 2-propanol oxidation is shifted accordingly, eventually leading to enhanced current densities recorded in a potential window where neither Rh/C nor Pd/C show similar activities. In the case of PtRu/C, the voltammograms between the alloy and the Pt monometallic surface show differences that cannot be easily explained without any additional operando characterization, based on X-ray spectroscopy. Nevertheless, it seems that the PtRu/C peak potential emerges at the same potential (ca. +0. 85 V_{RHE}) where the third oxidation stage initiates.

Product Analysis During Chronoamperometry

To further investigate the evolution of 2-propanol electrooxidation and the respective product formation over time, product analysis was conducted in real time with EC-RTMS at several constant potentials. We have previously shown that in alkaline conditions the sole product of the 2-propanol electrooxidation is acetone on polycrystalline noble metal electrodes, whereas C–C bond splitting or CO_{ads} formation on the surface was excluded, using electrochemical infrared reflection absorption spectroscopy (EC-IRRAS) measurements.[13]

The experimental protocol consisted of 5 min steps at a constant potential, which were separated by 3 min relaxation steps at 0 V_{RHE}, following the methodology that was previously developed by our group.[7] The latter step is crucial to prepare a reproducible surface by removing surface adsorbates (e.g. acetone) and reduce any previously formed oxide species, but also to ensure that the mass spectrometry signal for acetone, I_{ACE}, has reached the background level. The potential at each successive potentiostatic step was 100 mV more positive than that at the previous step. For each studied electrode (Pd/C, Rh/C, PdRh/C, Pt/C and PtRu/C), the chronoamperometric experiment was designed to cover the potential range where the respective surface is active for 2-propanol electrooxidation, as found from the LSVs.

The I_{ACE} signal shows a marginal difference from the background during the step at +0.1 V_{RHE} for Rh/C and PdRh/C, but it is clearly distinguished at the more positive step at +0.1 V_{RHE}, confirming that the early onset observed during the LSVs on these two catalysts is related to formation of acetone at low overpotential. Higher formation rates are detected at steps at +0.3 V_{RHE} and even more at +0.4 V_{RHE}, which are more prominent for PdRh/C, while they both decline from +0.5 V_{RHE} and above, all in line with the voltametric findings. On the other catalysts, the formation of acetone is observed only at more positive potentials. Similarly to our previous study, the oxidation rate decays with time regardless of the studied electrocatalyst or the applied potential,[13] as shown in Figure 5. This is apparent both from the current density versus time profiles (Figure 5B) and by the I_{ACE} intensities versus time (Figure 5A). The latter measurement utterly represents the acetone formation rate with time, as there is no charging

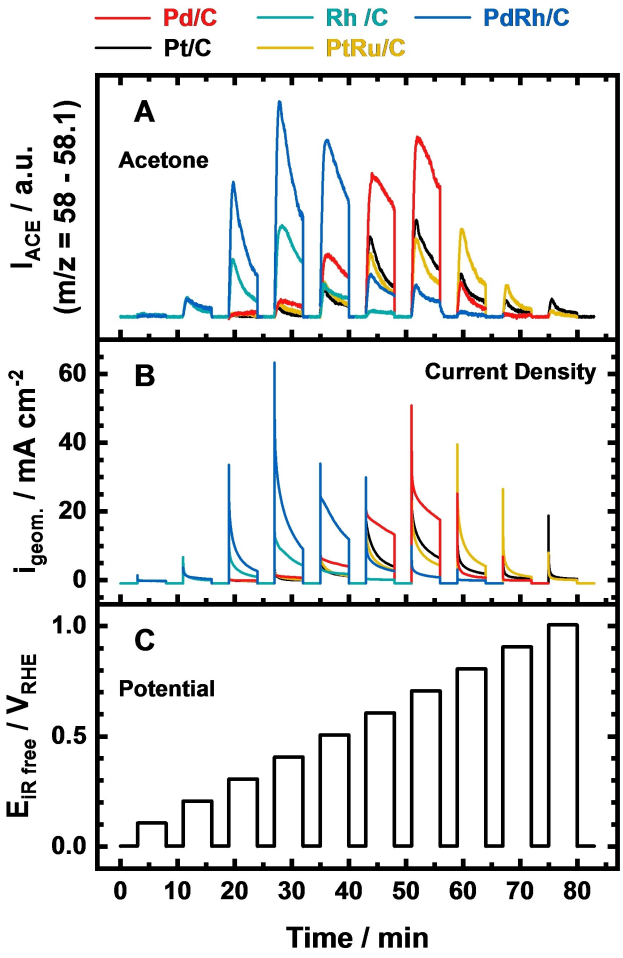

Figure 5. Chronoamperometric steps on Pd/C, Rh/C, PdRh/C, Pt/C and PtRu/C nanoparticles in a potential window from +0.1 to +1 V_{RHE} for 5 min, interrupted by steps at 0 V_{RHE} for 3 min, in 0.1 mol L^{-1} NaOH and 0.2 mol L^{-1} 2-propanol. The current densities and ion currents are shown for the aforementioned nanoparticle electrodes.

current effect during the potential switch. Additionally, mass transport limitations are considered negligible and not a possible origin for the rate decay, given the fact that the SFC was used for the chronoamperometric step measurements. Under this frame, the observed performance is attributed solely to gradual electrocatalyst deactivation, which is likely related to the concomitant formation and accumulation of acetone on the electrode surface. As described previously on platinum in acid using time-resolved infrared spectra, the produced acetone is not entirely desorbed from the surface, leading to a partial coverage with acetone which increases gradually with time (until an equilibrium coverage is reached at each potential), hindering the interaction of 2-propanol molecules with the electrode and leading to kinetic limitations.[17]

© 2025 The Authors. ChemElectroChem published by Wiley-VCH GmbH

21960216, 2025, 9, Downloaded from https://chemistry-europe.onlinelibrary.wiley.com/doi/10.1002/celc.202400699 by Forschungszentrum Jülich GmbH Research Center, Wiley Online Library on [08/12/2025]. See the Terms and Conditions (https://onlinelibrary.wiley.com/terms-and-conditions) on Wiley Online Library for rules of use; OA articles are governed by the applicable Creative Commons License

21960216, 2025, 9, Downloaded from https://chemistry-europe.onlinelibrary.wiley.com/doi/10.1002/celc.202400699 by Forschungszentrum Jülich GmbH Research Center, Wiley Online Library on [08/12/2025]. See the Terms and Conditions (https://onlinelibrary.wiley.com/terms-and-conditions) on Wiley Online Library for rules of use; OA articles are governed by the applicable Creative Commons License

Potential-Dependent Dissolution Rates for PdRh/C and PtRu/C

Stability of the carbon-supported PdRh and PtRu catalyst samples was screened by an on-line ICP-MS. This technique allows tracking the dissolution rates of each metal in the alloys in real time while running electrochemical protocols.[41] The dissolution characteristics of the monometallic surfaces have been previously studied, so here we focus on the stability of PdRh/C which was not investigated previously, as well as of PtRu/C for comparison.[30,55]

To identify the influence of 2-propanol on the dissolution kinetics, measurements were carried out both in 0.05 mol L^{-1} KOH and in 0.05 mol L^{-1} KOH + 0.05 mol L^{-1} 2-propanol. Results are presented in Figures 6A and 6C (the applied protocol is described in detail in the Materials and Methods section). While part of the potential windows tested here may be outside of the expected potentials at the anode of an alcohol fuel cell under steady operation, such values might occur for example, during the startup/shutdown sequence of the cell or if the electrolyte instantly depletes in alcohol. Thus, such high anodic potentials (ca. +1.0 to +1.2 V_{RHE}) are often set in several accelerated degradation protocols in fundamental studies.[56]

The first feature, which is visible in the case of all metals during the potentiostatic hold, appears when the SFC gets in contact with the working electrode and corresponds to the dissolution of native oxides, inherently present at the catalyst surface, especially when the catalysts were stored under air.[57] The presence of 2-propanol had a striking influence on the size of the contact peaks in the case of Pd, Rh and Pt leading to significantly higher dissolution rates compared to the propanol-free 0.05 mol L^{-1} KOH case. The reason behind this phenomenon is yet to be uncovered, but 2-propanol can clearly alter the stability of the given metal negatively. One possible explanation could be that the adsorption of 2-propanol may suppress the redeposition of the dissolved species, as has been shown in the case of CO.[58]

Pd dissolution is evident even at the lowest, +1 V_{RHE} upper potential limit (Figures 6A, 6B and on a linear scale in Figure S3A, in the SI). The onset potential of dissolution is ca. +0.87 V_{RHE}, which matches well with the values published in the literature under similar conditions, along with the number and shape of the two main dissolution features.[55] The first one corresponds to the formation of PdO_x, while the second, cathodic dissolution peak corresponds to the reduction of the previously formed oxide; both processes are accompanied with

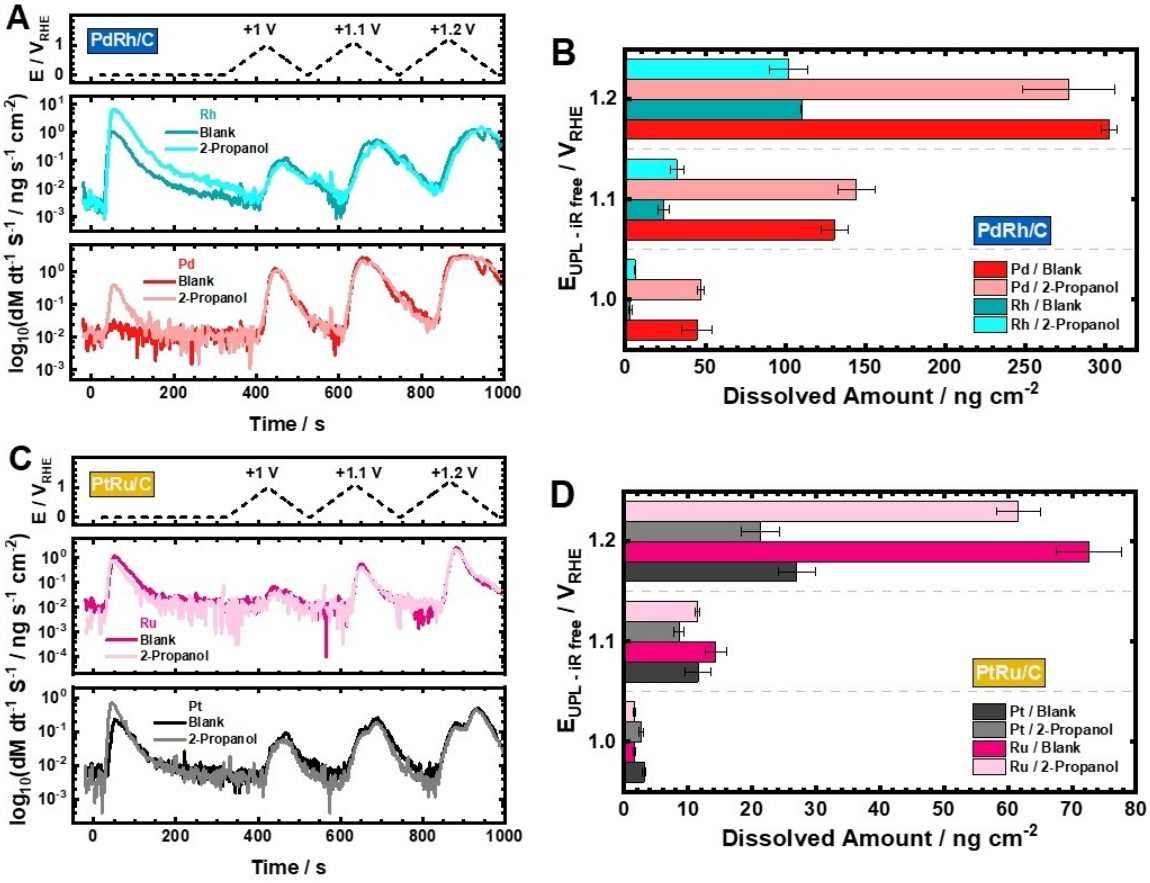

Figure 6. Dissolution rates of Pd and Rh for PdRh/C catalyst (A) and dissolution rates of Pt and Ru for PtRu/C catalyst (C) recorded during a protocol consisting of three CVs with increasing upper potential limit from +1.0 to +1.2 V_{RHE} ($\Delta E = 0.1$ V, $\upsilon = 10$ mV s^{-1}) in either 0.05 mol L^{-1} KOH or in 0.05 mol L^{-1} KOH + 0.05 mol L^{-1} 2-propanol electrolyte solutions. Dissolved amount of Pd and Rh (B), or Pt and Ru (D) in a cycle. Dissolved amounts were obtained by integrating the dissolution features presented in (A) and (C). Logarithmic scale was used for better visibility of dissolution peaks; see Figures S3A and S3B for linear scale. Error bars were calculated from at least two measurements; each performed on a fresh catalyst location.

© 2025 The Authors. ChemElectroChem published by Wiley-VCH GmbH

Pd dissolution. The two dissolution peaks are merged into one feature; cathodic dissolution appeared as a discernable shoulder (especially in the case of the highest upper potential limit). The amount of Pd dissolving cathodically remains smaller than the anodically dissolved, until the upper potential limit reaches $+1.2\ V_{RHE}$. Here, the cathodic dissolution rates are in the same ballpark as anodic dissolution. The addition of 2-propanol did not affect the onset potential of dissolution. On the other hand, when the upper potential limit was increased to $+1.2\ V_{RHE}$, anodic and cathodic dissolution features cannot be separated, however, the magnitude of the dissolution rates remained similar.

Rh dissolution started at $+0.82\ V_{RHE}$ (Figures 6A and 6B). Similar to the case of Pd, two dissolution peaks can be spotted. The anodic dissolution corresponds to the oxidation of Rh accompanied by Rh dissolution. Based on the Pourbaix diagram, various solid-oxide transformations are possible, resulting in either Rh_2O or Rh_2O_3.[59] The cathodic Rh dissolution feature emerged due to the reduction of the Rh oxide layer. Similarly to Pd, dissolution rates are unaffected by 2-propanol, alongside the convolution of cathodic and anodic dissolution features, at the highest upper potential limit.

As a control experiment besides PdRh, the stability of PtRu was also studied (Figures 6C, 6D and on a linear scale in Figure S3B, in the SI). Pt and Ru dissolution starts almost at the same potentials, $+0.98\ V_{RHE}$ and $+1\ V_{RHE}$, respectively. The oxidation of Pt manifested in a transient anodic dissolution feature due to PtO_x formation, while the reduction of the surface oxide layer leads to the formation of a cathodic dissolution peak. Dissolution rates are always smaller in the case of anodic dissolution. In contrast, anodic and cathodic Ru dissolution features are only visible when the upper potential limit is $+1\ V_{RHE}$ corresponding to the formation of various Ru oxides ($RuO_2 \cdot H_2O$, $Ru(OH)_3$);[30,59] anodic and cathodic dissolution peaks are merged. Dissolution rates are slightly lower in the presence of 2-propanol both for Pt and Ru. The onset potential of dissolution was not affected by the addition of 2-propanol for all four investigated metals.

Dissolved amounts were always calculated by integrating dissolution peaks that appeared during a whole cyclic voltammogram in consecutive cycles by increasing the upper limit potential each time (Figures 6B and 6D). As it is visible in Figure 6B, the amount of dissolved Pd is significantly higher than the values obtained for Rh ranging from $\approx$45–300 $ng_{Pd}\,cm^{-2}$ for upper limits from $+1.0$ to $+1.2\ V_{RHE}$, while Rh dissolution even at the highest upper potential limit did not exceed 110 $ng_{Rh}\,cm^{-2}$. The other, important conclusion is that the addition of 2-propanol did not destabilize further Pd and Rh; the dissolved amount is identical within the margin of error.

In the case of the PtRu/C sample, the amount of dissolved Ru was first lower ($+1\ V_{RHE}$ upper potential limit), similar ($+1.1\ V_{RHE}$) and notably higher ($+1.2\ V_{RHE}$) compared to Pt. The calculated dissolved amounts are approximately 4–5 times lower compared to the values gathered for the PdRh/C system. The addition of 2-propanol slightly decreased the dissolved amounts of Pt and Ru especially at the two higher upper potential limits. Similar trends were observed earlier for PtRu/C both in acidic and alkaline media. The increase in stability was tied to the 2-propanol oxidation product, acetone, irreversibly adsorbing at the PtRu surface.[30] However, in this study, the increase in stability is somewhat lower compared to previous reports.[7,30] We attribute this deviation to the higher dissolution rates experienced during contacting the working electrode that affects the concomitant dissolution rates at higher upper limit potentials.

Conclusions

2-propanol fuel cells can be used to harvest the hydrogen stored in LOHCs to generate electricity by oxidizing 2-propanol to acetone at the anode and hydrogenating the latter from an LOHC molecule back to 2-propanol in a catalytic reactor. In acidic electrolytes, which is relevant for PEMFC applications and where most work has focused on so far, the choice of anode materials is limited to platinum-based electrodes due to the inactivity of other noble metal-based catalysts and the poor stability of non-noble metals under the operating conditions. In this work, we evaluate the performance of various carbon-supported mono- and bi-metallic nanoparticles based on noble metals in an alkaline electrolyte, with an outlook to an application in an alkaline fuel cell.

Data from linear sweep voltammetry show that the onset of the reaction on PtRu/C, Rh/C and PdRh/C is as low as the thermodynamic equilibrium potential for the acetone/2-propanol redox couple, but a much higher maximum current is recorded for PdRh/C compared to the other two catalysts, whereas Pd/C and Pt/C show a much higher onset potential, making PdRh/C the most promising catalyst for a 2-propanol alkaline fuel cell operation. Electrochemical real-time mass spectrometry showed that acetone is formed on all catalysts studied, in line with previous studies on polycrystalline electrodes in the same solution as well as in acid.

After calculation of the TEM-derived surface area of the different catalysts, we find that the differences in current recorded for the various materials are not related to differences in particle size or the active surface area exposed to the electrolyte, but instead they should be attributed to intrinsic characteristics of the respective catalyst.

Using online dissolution monitoring with ICP-MS, we find that all metals in the studied catalysts can dissolve in either the presence or the absence of 2-propanol during both the forward and the backward scan, if they are exposed to sufficiently high potentials that can be relevant during dynamic, startup/shutdown operation. The extent of the cathodic and anodic dissolution depends on the highest applied potential. Even though the deactivation of all catalysts derives mainly either from acetone accumulation or surface oxidation, for the most promising case, PdRh/C, the dissolution results suggest that the anode potential in a 2-propanol alkaline fuel cell should not exceed ca. $+0.8$ V during transient operation, i.e., during startup/shutdown or idle conditions, otherwise both palladium

© 2025 The Authors. ChemElectroChem published by Wiley-VCH GmbH

21960216, 2025, 9, Downloaded from https://chemistry-europe.onlinelibrary.wiley.com/doi/10.1002/celc.202400699 by Forschungszentrum Jülich GmbH Research Center, Wiley Online Library on [08/12/2025]. See the Terms and Conditions (https://onlinelibrary.wiley.com/terms-and-conditions) on Wiley Online Library for rules of use; OA articles are governed by the applicable Creative Commons License

and rhodium can dissolve and affect the long-term performance of the fuel cell.

Author Contributions

The authors contributed as follows: Iosif Mangoufis-Giasin: Conceptualization, Methodology, Validation, Formal Analysis, Investigation, Data Curation, Writing – Original Draft, Visualization. Attila Kormányos: Resources, Investigation, Writing – Review & Editing. Mária Minichová: Resources, Writing – Review & Editing, Investigation. Andreas Körner: Resources, Writing – Review & Editing. Birk Fritsch: Resources, Writing – Review & Editing. Karl J.J. Mayrhofer: Writing – Review & Editing, Project Administration, Funding Acquisition. Serhiy Cherevko: Writing – Review & Editing. Ioannis Katsounaros: Methodology, Writing – Review & Editing, Supervision.

Acknowledgements

This work was funded by the Bavarian Ministry of Economic Affairs, Regional Development and Energy.

Conflict of Interests

The authors declare no conflict of interest.

Data Availability Statement

The data that support the findings of this study are available from the corresponding author upon reasonable request.

Keywords: Hydrogen economy · Liquid organic hydrogen carriers · 2-propanol oxidation · Alcohol fuel cell anodes · Alkaline media

[1] D. Teichmann, W. Arlt, P. Wasserscheid, R. Freymann, *Energy Environ. Sci.* **2011**, *4*, 2767.
[2] N. Brückner, K. Obesser, A. Bösmann, D. Teichmann, W. Arlt, J. Dungs, P. Wasserscheid, *ChemSusChem* **2014**, *7*, 229.
[3] P. Preuster, C. Papp, P. Wasserscheid, *Acc. Chem. Res.* **2017**, *50*, 74.
[4] G. Sievi, D. Geburtig, T. Skeledzic, A. Bösmann, P. Preuster, O. Brummel, F. Waidhas, M. A. Montero, P. Khanipour, I. Katsounaros, J. Libuda, K. J. J. Mayrhofer, P. Wasserscheid, *Energy Environ. Sci.* **2019**, *12*, 2305.
[5] P. Preuster, Q. Fang, R. Peters, R. Deja, V. N. Nguyen, L. Blum, D. Stolten, P. Wasserscheid, *Int. J. Hydrogen Energy* **2018**, *43*, 1758.
[6] S. Sen Gupta, J. Datta, *J. Chem. Sci.* **2005**, *117*, 337.
[7] P. Khanipour, F. D. Speck, I. Mangoufis-Giasin, K. J. J. Mayrhofer, S. Cherevko, I. Katsounaros, *ACS Appl. Mater. Interfaces* **2020**, *12*, 33670.
[8] E. Pastor, S. González, A. J. Arvia, *J. Electroanal. Chem.* **1995**, *395*, 233.
[9] S. G. Sun, Y. Lin, *J. Electroanal. Chem.* **1994**, *375*, 401.
[10] S. G. Sun, D. F. Yang, Z. W. Tian, *J. Electroanal. Chem.* **1990**, *289*, 177.
[11] S. G. Sun, Y. Lin, *Electrochim. Acta* **1996**, *41*, 693.
[12] S.-G. Sun, Y. Lin, *Electrochim. Acta* **1998**, *44*, 1153.
[13] I. Mangoufis-Giasin, L. Fusek, T. Yang, P. Khanipour, O. Brummel, J. Libuda, K. J. J. Mayrhofer, F. Calle-Vallejo, I. Katsounaros, *ACS Catal.* **2023**, *13*, 14562.
[14] J. F. E. Gootzen, A. H. Wonders, W. Visscher, J. A. R. Van Veen, *Langmuir* **1997**, *13*, 1659.
[15] I. D. A. Rodrigues, J. P. I. De Souza, E. Pastor, F. C. Nart, *Langmuir* **1997**, *13*, 6829.
[16] J. F. Gomes, V. L. Oliveira, P. M. P. Pratta, G. Tremiliosi-Filho, *Electrocatalysis* **2015**, *6*, 7.
[17] F. Waidhas, S. Haschke, P. Khanipour, L. Fromm, A. Görling, J. Bachmann, I. Katsounaros, K. J. J. Mayrhofer, O. Brummel, J. Libuda, *ACS Catal.* **2020**, *10*, 6831.
[18] I. Mangoufis-Giasin, O. Piqué, P. Khanipour, K. J. J. Mayrhofer, F. Calle-Vallejo, I. Katsounaros, *J. Catal.* **2021**, *400*, 166.
[19] T. Yang, J. Yang, X. Deng, E. Franz, L. Fromm, N. Taccardi, Z. Liu, A. Görling, P. Wasserscheid, O. Brummel, J. Libuda, *Angew. Chem. - Int. Ed.* **2022**, *61*, 1.
[20] M. E. P. Markiewicz, D. M. Hebert, S. H. Bergens, *J. Power Sources* **2006**, *161*, 761.
[21] D. Cao, S. H. Bergens, *J. Power Sources* **2003**, *124*, 12.
[22] Y. Liu, Y. Zeng, R. Liu, H. Wu, G. Wang, D. Cao, *Electrochim. Acta* **2012**, *76*, 174.
[23] A. Santasalo-Aarnio, Y. Kwon, E. Ahlberg, K. Kontturi, T. Kallio, M. T. M. Koper, *Electrochem. Commun.* **2011**, *13*, 466.
[24] T. Okanishi, Y. Katayama, R. Ito, H. Muroyama, T. Matsui, K. Eguchi, *Phys. Chem. Chem. Phys.* **2016**, *18*, 10109.
[25] J. Ye, J. Liu, C. Xu, S. P. Jiang, Y. Tong, *Electrochem. Commun.* **2007**, *9*, 2760.
[26] Y. Choi, I. Sinev, H. Mistry, I. Zegkinoglou, B. Roldan Cuenya, *ACS Catal.* **2016**, *6*, 3396.
[27] S. Xing, Z. Liu, Q. Xue, S. Yin, F. Li, W. Cai, S. Li, P. Chen, P. Jin, H. Yao, Y. Chen, *Appl. Catal. B Environ.* **2019**, *259*, 118082.
[28] F. Cheng, H. Wang, Z. Sun, M. Ning, Z. Cai, M. Zhang, *Electrochem. Commun.* **2008**, *10*, 798.
[29] J. Van Drunen, T. W. Napporn, B. Kokoh, G. Jerkiewicz, *J. Electroanal. Chem.* **2014**, *716*, 120.
[30] A. Kormányos, F. D. Speck, K. J. J. Mayrhofer, S. Cherevko, *ACS Catal.* **2020**, *10*, 10858.
[31] A. Santasalo-Aarnio, S. Tuomi, K. Jalkanen, K. Kontturi, T. Kallio, *Electrochim. Acta* **2013**, *87*, 730.
[32] Y. Feng, Z. Li, C. Huang, Y. Wang, *Ionics* **2011**, *17*, 617.
[33] Y. Feng, W. Yin, Z. Li, C. Huang, Y. Wang, *Electrochim. Acta* **2010**, *55*, 6991.
[34] Y. Cheng, Y. Liu, D. Cao, G. Wang, Y. Gao, *J. Power Sources* **2011**, *196*, 3124.
[35] C. Xu, Z. Tian, Z. Chen, S. P. Jiang, *Electrochem. Commun.* **2008**, *10*, 246.
[36] W. Zhou, C. Wang, J. Xu, Y. Du, P. Yang, *Mater. Chem. Phys.* **2010**, *123*, 390.
[37] A. Serov, U. Martinez, A. Falase, P. Atanassov, *Electrochem. Commun.* **2012**, *22*, 193.
[38] A. Zalineeva, A. Serov, M. Padilla, U. Martinez, K. Artyushkova, S. Baranton, C. Coutanceau, P. Atanassov, *Electrochem. Commun.* **2015**, *57*, 48.
[39] W. Wang, S. Liu, Y. Wang, W. Jing, X. Niu, Z. Lei, *Int. J. Hydrogen Energy* **2018**, *43*, 15952.
[40] P. Khanipour, *Electrochemical real-time mass spectrometry: A novel tool for time-resolved characterization of the products of electrochemical reaction*, PhD thesis, Friedrich-Alexander-Universität Erlangen-Nürnberg (DE), **2020**, https://open.fau.de/items/a1e32675-73cd-40e3-8eff-4373887adb8b.
[41] O. Kasian, S. Geiger, K. J. J. Mayrhofer, S. Cherevko, *Chem. Rec.* **2019**, *19*, 2130.
[42] S. O. Klemm, A. A. Topalov, C. A. Laska, K. J. J. Mayrhofer, *Electrochem. Commun.* **2011**, *13*, 1533.
[43] H. G. Merkus, *Particle Size Measurements - Fundamentals, Practice, Quality*, Springer, **2009**, p. 13–42.
[44] A. Simanenko, P. K. Samal, R. Hübsch, J. Škvára, J. Yang, M. Kastenmeier, F. Winkler, T. Skála, N. Tsud, S. Mehl, J. Mysliveček, O. Brummel, Y. Lykhach, J. Libuda, *ACS Energy Lett.* **2024**, *9*, 4875.
[45] P. A. Loichet Torres, Y.-S. Li, C. Grön, T. Lazaridis, P. Watermeyer, N. Cheng, C. H. Liebscher, H. A. Gasteiger, *J. Electrochem. Soc.* **2023**, *170*, 124503.
[46] E. Antolini, L. Giorgi, F. Cardellini, E. Passalacqua, *J. Solid State Electrochem.* **2001**, *5*, 131.
[47] W. Zhou, M. Li, O. L. Ding, S. H. Chan, L. Zhang, Y. Xue, *Int. J. Hydrogen Energy* **2014**, *39*, 6433.
[48] S. Zhang, X. Zhang, Y. Zhu, N. Sun, J. Qin, R. Liu, *Solid State Commun.* **2014**, *189*, 43.

© 2025 The Authors. ChemElectroChem published by Wiley-VCH GmbH

21960216, 2025, 9, Downloaded from https://chemistry-europe.onlinelibrary.wiley.com/doi/10.1002/celc.202400699 by Forschungszentrum Jülich GmbH Research Center, Wiley Online Library on [08/12/2025]. See the Terms and Conditions (https://onlinelibrary.wiley.com/terms-and-conditions) on Wiley Online Library for rules of use; OA articles are governed by the applicable Creative Commons License

[49] D. Čukman, M. Vuković, *J. Electroanal. Chem.* **1990**, *279*, 273.
[50] V. Galvan, D. E. Glass, A. F. Baxter, G. K. Surya Prakash, *ACS Appl. Energy Mater.* **2019**, *2*, 7104.
[51] L. Geniès, R. Faure, R. Durand, *Electrochim. Acta* **1998**, *44*, 1317.
[52] Z. X. Liang, T. S. Zhao, J. B. Xu, L. D. Zhu, *Electrochim. Acta* **2009**, *54*, 2203.
[53] M. Peuckert, *Electrochim. Acta* **1984**, *29*, 1315.
[54] M. Favaro, C. Valero-Vidal, J. Eichhorn, F. M. Toma, P. N. Ross, J. Yano, Z. Liu, E. J. Crumlin, *J. Mater. Chem. A* **2017**, *5*, 11634.
[55] M. Schalenbach, O. Kasian, M. Ledendecker, F. D. Speck, A. M. Mingers, K. J. J. Mayrhofer, S. Cherevko, *Electrocatalysis* **2018**, *9*, 153.
[56] N. Hodnik, P. Jovanovič, A. Pavlišič, B. Jozinović, M. Zorko, M. Bele, V. S. Šelih, M. Šala, S. Hočevar, M. Gaberšček, *J. Phys. Chem. C* **2015**, *119*, 10140.
[57] S. Cherevko, *J. Electroanal. Chem.* **2017**, *787*, 11.
[58] A. A. Topalov, A. R. Zeradjanin, S. Cherevko, K. J. J. Mayrhofer, *Electrochem. Commun.* **2014**, *40*, 49.
[59] M. Pourbaix, *Atlas of Electrochemical Equilibria in Aqueous Solutions*, NACE International, Houston **1974**, pp. 343–383.

Manuscript received: December 18, 2024
Revised manuscript received: January 30, 2025
Version of record online: March 18, 2025

© 2025 The Authors. ChemElectroChem published by Wiley-VCH GmbH

21960216, 2025, 9, Downloaded from https://chemistry-europe.onlinelibrary.wiley.com/doi/10.1002/celc.202400699 by Forschungszentrum Jülich GmbH Research Center, Wiley Online Library on [08/12/2025]. See the Terms and Conditions (https://onlinelibrary.wiley.com/terms-and-conditions) on Wiley Online Library for rules of use; OA articles are governed by the applicable Creative Commons License